Supporting Information for

Emergent Inductance in Antiferromagnetic Systems with Spin-orbit Coupling

Shiqi Wang[1], Daoqian Zhu[1,2*], Yuhao Jiang[1], Ao Du[1] and Weisheng Zhao[1,2*]

1. Fert Beijing Institute, School of Integrated Circuit Science and Engineering, Beihang University, Beijing 100191, China.

2. National Key Lab of Spintronics, Institute of International Innovation, Beihang University, Yuhang District, Hangzhou 311115, China.

* Corresponding author:
daoqian_zhu@buaa.edu.cn; weisheng.zhao@buaa.edu.cn

Supplementary Note 10: Quantitative scaling law of $J_{e,th}$ under different frequency and material parameters

Supplementary Note 11: Discussion of the emergence of higher harmonics terms and its impact on emergent inductance

Supplementary Note 12: Compatibility analysis of AFM emergent inductor with AFM memory technologies

Supplementary Note 13: Comparison of the emergent inductance in SOC-FM systems and SOC-AFM systems under external magnetic field

Supplementary Note 14: Simulation details of emergent inductance under external magnetic field in SOC-FM systems

Supplementary Note 1: Current device design connecting SOT-induced AFM dynamics with alternating signal output

There are some previous works which could combine spin-orbit torque (SOT)-induced AFM precession and alternating/inductive electrical signal contributed by AFM dynamics. The core concepts of these works are introduced as below.

In Ref. 1, the concept of AFM spin pumping (SP) is constructed. The AFM dynamics could be activated by SHE-induced SOT in adjacent heavy metal (HM) layer[2] or SOT in material itself[3,4], spin current proportional to $n \times \frac{\partial n}{\partial t}$ will be pumped out accordingly and conversed into charge current in adjacent HM layer by ISHE[2,5] or in material itself by IREE[3,4]. In Ref. 4, the alternating conductivity and effective reactance from this process are systematically discussed based on antiferromagnetic topological insulator with different septuple-layers and different sublattice SOT. However, inductive behaviour with positive reactance is only found above antiferromagnetic resonance frequency f_{AFMR}, while we expect to observe it in low frequency region (below f_{AFMR}).

In Ref. 6, the concept of AFM Spin-Hall Nano-Oscillator (SHNO) was proposed in theory. Here SOT is generated by Spin Hall Effect (SHE) in adjacent heavy metal with strong SOC. The damping-like torque term with the form of $m_i \times (m_i \times \sigma)$ will compensate with the Gilbert damping torque under a certain value of direct current injection and external magnetic field. Stable AFM precession will be realized accordingly and the alternating signal could be read out by ISHE from SP process[7] or Anomalous Hall Effect (AHE)[8]. However, the concept could not be seen as inductor device since the current injection should be alternating and change with time.

In Ref. 9 and Ref. 10, locally excited and detected AFM spin wave (SW) was successfully demonstrated in experiments. Spin wave could be excited by DC-SOT in adjacent HM layer[9], while the detection could be completed in AC method based on electromagnetic induction (EMI) between micro-wave magnetic field generated by AFM dynamics and induced electric current in adjacent inductive antenna[10]. Specifically, divided route of signal excitation and detection is usually involved and necessary, while the inductor needs a multiplexing structure.

As discussed above, these device concepts could not work as ideal inductors from various aspects, while our device's concept could fulfil these aspects well. The main differences between our device's concept and all the works above are summarized in TABLE SI. In this work, the emergent inductance is generated by spin motive force with SOC origin, and the AFM dynamics is motivated by SOT under alternating current injection. The generated voltage is alternating with time, is proportional to frequency in magnitude and shows 90° phase difference with input current in low frequency below f_{AFMR}, all of which fit the inductive behaviour well. The concept can be demonstrated by a single nano-scale deice with an excitation-detection multiplexing route, and could be realized in metal AFM material Mn_2Au with low resistivity (20 $\mu\Omega \cdot cm$). All of the features above make our device concept an ideal choice for inductor.

TABLE SI Comparison between different device concepts connecting SOT-induced AFM dynamics and induced alternating output signal.

Device concept	Stimulus method	Origin of AC-output signal	Phase difference I_{in} v.s. V_{out}	Multiplexing excitation & detection?
SP[1]	AC-SOT[2-5]	ISHE[2,5]/IREE[3,4]	-90° for $f > f_{AFMR}$[4]	Yes
SHNO[6]	DC-SOT[7,8]	ISHE[7]/AHE[8]	/	Yes for ISHE[7]
SW[9,10]	DC-SOT[9]/AC-Magnetic Field[10]	EMI[10]	/	No
This work*	AC-SOT	SMF from SOC	-90° for $f < f_{AFMR}$	Yes

Supplementary Note 2: Relationship between the sign of sublattice SOC and the breaking of structure symmetry

The incorporation of Rashba-SOC into AFM systems needs the existence of broken inversion symmetry[11,12], specifically, the structural inversion symmetry breaking (ISB) in either global type or local type. The former usually applies to globally centrosymmetric AFM structures (each sublattice owns structural symmetry), such as PtMn as shown in Fig. S1(a).[13] In this case, the generation of Rashba-SOC relies on the external broken structural symmetry when AFM is adjacent to another material with different work function, such as MgO[14]. The sign of Rashba-SOC and the chirality of spin textures are identical in each AFM sublattice due to the same structural breaking direction, as shown in the bottom panel of Fig. S1(a).

The latter refers to AFM systems in which the structural symmetry is broken locally and towards opposite direction in each sublattice, while the bulk centrosymmetry could still be kept.[11,12] Here we take the candidate structure Mn_2Au as an example. As shown in Fig. S1(b), the full crystal is centrosymmetric around the highlighted Au atom in blue circle, but the inversion symmetry of Mn_A atom (AFM sublattice A) and Mn_B atom (AFM sublattice B) is oppositely broken along c axis (z axis). This is attributed to different layer staking order for Mn_A atom and Mn_B atom (the nearest Au layer is beneath Mn_A atom while on top of Mn_B atom). Consequently, the sublattice Rashba-SOC and the chirality of spin textures are opposite to each other in this structure, as shown in the bottom panel of Fig. S1(b).

The two situations above correspond to the situation of uniform ($\eta_1 = \eta_2 = +1$) and staggered ($\eta_1 = -\eta_2 = +1$) spin accumulation in each AFM sublattices, while it was indicated that nonequal spin accumulation modeled by $0 \leq |\eta_1| \neq |\eta_2| \leq 1$ could also be common in colinear AFM systems[15]. This could be realized by either the disbalance of external spin current injection in two sublattices, or by asymmetric sublattice Rashba-SOC combing both global and local types of structural ISB, as shown in Fig. S1(c). Atoms in the Mn_B sublattice near the Mn_2Au/MgO interface experience a competition between the intrinsic local ISB of Mn_2Au and the extrinsic global ISB induced by the MgO interface. In contrast, the upper-layer Mn_A atoms are subject only to the intrinsic local ISB. This disparity results in asymmetric spin textures characterized by strong left-handed chirality in sublattice A with $\eta_1 = +1$ and relatively weak right-handed chirality in sublattice B, which even undergo a crossover to left-handness with $-1 < \eta_2 < +1$. Non-equivalent spin accumulations between the two sublattices could be thus realized.

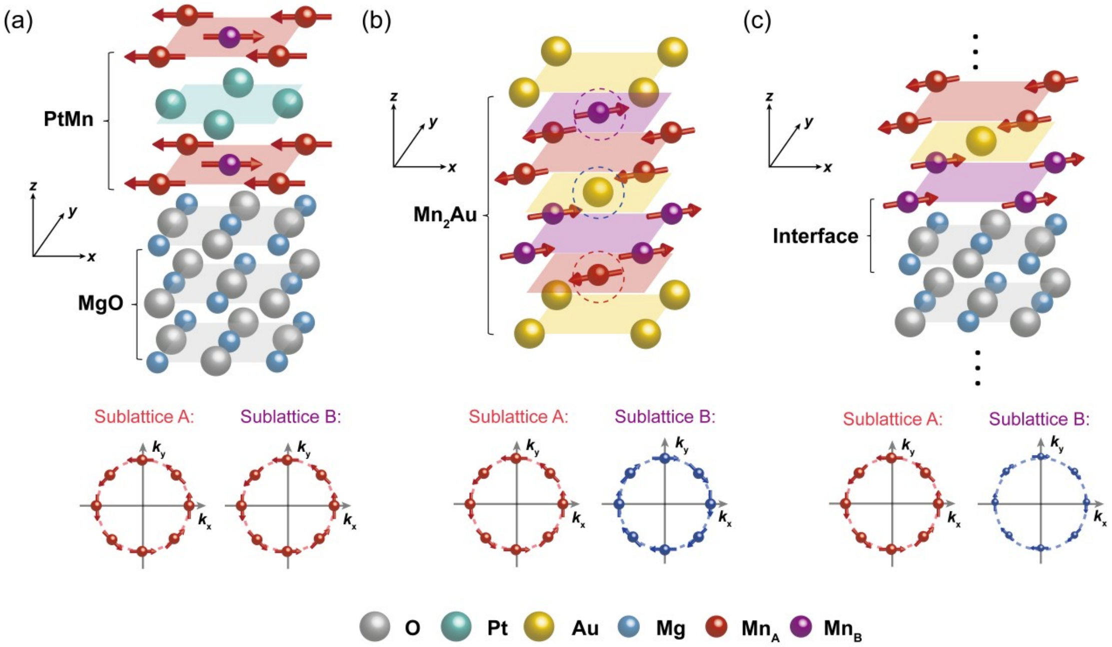

FIG. S1. Crystal structures (top) and corresponding sublattice Rashba spin textures (bottom) of (a) PtMn/MgO, (b) Mn_2Au, and (c) Mn_2Au/MgO. (a) In the PtMn/MgO heterostructure, the global ISB strictly at the MgO interface induces spin textures with identical chirality and identical intensity for both Mn_A and Mn_B sublattices. (b) Mn_2Au is globally centrosymmetric (around Au atom, blue dotted circle) but possesses opposite local ISB at Mn_A (red dotted circle) and Mn_B (purple dotted circle) sites, generating spin textures with opposite chirality but identical intensity. (c) In Mn_2Au/MgO, the competition between the intrinsic local ISB of Mn_2Au and the extrinsic global ISB from the MgO interface leads to non-equal spin textures (different chirality/intensity) between the two sublattices.

Supplementary Note 3: Detailed formula derivation of $\frac{\partial m_i}{\partial t}$ and spin motive force

In Methodology, we assume an alternating electric current with current density $j_e = j_\omega e^{i\omega t}$ and angular frequency $\omega = 2\pi f$ is applied into our prototype device. The input electric current will generate alternating SOT and will drive the magnetization dynamics $m_i = m_{i,0} + \tilde{m}_{i,\omega} e^{i\omega t}$. Here, $m_{i,0}$ is the time-independent part and $\tilde{m}_{i,\omega}$ is the complex amplitude of magnetization precession. Further, we have $m_i \simeq m_{i,0}\hat{x} + e^{i\omega t}(\tilde{m}_{i,\omega}^{y}\hat{y} + \tilde{m}_{i,\omega}^{z}\hat{z})$ with $m_{i,0} = \pm 1$ and $|\tilde{m}_{i,\omega}^{y,z}| \ll 1$ under the assumption of zero external magnetic field and sufficiently small SOT (compared with the exchange torque). If $m_{1,0} = 1$ and $m_{2,0} = -1$, the coupled LLG equation can be reduced to:

$$\begin{cases} i\omega\tilde{m}_{1,\omega}^{y} + (\gamma\mu_0 H_E + \gamma\mu_0 H_K + \alpha i\omega)\tilde{m}_{1,\omega}^{z} + \gamma\mu_0 H_E \tilde{m}_{2,\omega}^{z} = 0 \\ -(\gamma\mu_0 H_E + \gamma\mu_0 H_K + \alpha i\omega)\tilde{m}_{1,\omega}^{y} + i\omega\tilde{m}_{1,\omega}^{z} - \gamma\mu_0 H_E \tilde{m}_{2,\omega}^{y} = -\gamma\mu_0 H_{SOC,1} cos\varphi \\ -\gamma\mu_0 H_E \tilde{m}_{1,\omega}^{z} + i\omega\tilde{m}_{2,\omega}^{y} - (\gamma\mu_0 H_E + \gamma\mu_0 H_K + \alpha i\omega)\tilde{m}_{2,\omega}^{z} = 0 \\ \gamma\mu_0 H_E \tilde{m}_{1,\omega}^{y} + (\gamma\mu_0 H_E + \gamma\mu_0 H_K + \alpha i\omega)\tilde{m}_{2,\omega}^{y} + i\omega\tilde{m}_{2,\omega}^{z} = \gamma\mu_0 H_{SOC,2} cos\varphi \end{cases} \#(S1)$$

Reviewing the Eq. (2) in the manuscript, we find that only the precession in ***y*** direction for sublattice magnetization will contributes to the SMF, because the ***x*** component of m_i is assumed to keep unchanged here. Combining Eq. (S1), we obtain the following solutions for $\tilde{m}_{1,\omega}^{y}$ and $\tilde{m}_{2,\omega}^{y}$:

$$\begin{cases} \tilde{m}_{1,\omega}^{y} = \dfrac{P\alpha_R j_\omega - \gamma(\gamma\mu_0 H_E(\eta_1 - \eta_2) + \gamma\mu_0 H_K \eta_1 + \alpha i\omega\eta_1)cos\varphi}{\mu_B M_S \qquad \omega^2 - \omega_{AFMR}^2 - 2i\Delta\omega} \\ \tilde{m}_{2,\omega}^{y} = \dfrac{P\alpha_R j_\omega - \gamma(\gamma\mu_0 H_E(\eta_2 - \eta_1) + \gamma\mu_0 H_K \eta_2 + \alpha i\omega\eta_2)cos\varphi}{\mu_B M_S \qquad \omega^2 - \omega_{AFMR}^2 - 2i\Delta\omega} \end{cases} \#(S2)$$

Then $\frac{\partial m_{i,y}}{\partial t}$ could be obtained by $i\omega\tilde{m}_{i,\omega}^{y} e^{i\omega t}$, which further leads to the analytical formula of SMF after substituting Eq. (S2) into Eq. (2):

$$\varepsilon_{SMF} = \frac{P^2\alpha_R^2 m_e l_d j_\omega \gamma[(\gamma\mu_0(H_E + H_K)i\omega - \alpha\omega^2)(\eta_1^2 + \eta_2^2) - 2\eta_1\eta_2\gamma\mu_0 H_E i\omega]}{2e\hbar\mu_B M_S \qquad \omega^2 - \omega_{AFMR}^2 - 2i\Delta\omega} cos^2\varphi e^{i\omega t} \#(S3)$$

Supplementary Note 4: Comparison of emergent inductance under different sublattice SOC configuration

According to $\tilde{L} =- \frac{\varepsilon_{SMF}}{dI/dt}$, the emergent inductance $\tilde{L}$ could be written by:

$$\begin{cases} Re(\tilde{L}) = \frac{P^2\alpha_R^2 m_e}{2\mu_B M_S e\hbar S_c} \frac{l_d\gamma^2\mu_0((H_E + H_K)(\eta_1^2 + \eta_2^2) - 2\eta_1\eta_2 H_E)\left(\omega_{AFMR}^2 -\right.}{(\omega_{AFMR}^2 - \omega^2)^2 + 4\Delta^2\omega^2} \\ Im(\tilde{L}) =- \frac{P^2\alpha_R^2 m_e}{2\mu_B M_S e\hbar S_c} \frac{l_d\gamma\alpha\omega[(\omega^2 + \gamma^2\mu_0^2 H_K^2)(\eta_1^2 + \eta_2^2) + 2\gamma^2\mu_0^2(\eta_1 - \eta_2)^2(H}{(\omega_{AFMR}^2 - \omega^2)^2 + 4\Delta^2\omega^2} \end{cases}$$

In low frequency region with $\omega \ll \omega_{AFMR}$, $Im(\tilde{L})$ will disappear and the Eq. (S4) can be thus reduced to:

$$L = \frac{P^2\alpha_R^2 m_e}{2\mu_B\mu_0 M_S e\hbar S_c} \frac{l_d((H_E + H_K)(\eta_1^2 + \eta_2^2) - 2\eta_1\eta_2 H_E)}{H_K(H_K + 2H_E)} cos^2\varphi \#(S5)$$

If we have identical SOC in two sublattices ($\eta_1 = \eta_2 =+ 1$), Eq. (S5) can be reduced to:

$$L_{\eta_1 = \eta_2} = \frac{P^2\alpha_R^2 m_e}{\mu_B\mu_0(2H_E + H_K)M_S e\hbar S_c} l_d cos^2\varphi \#(S6)$$

If we have asymmetric sublattice SOC such as $\eta_1 =+ 1$ and $\eta_2 = 0$, Eq. (S5) can be reduced to:

$$L_{|\eta_1| \neq |\eta_2|} = \frac{P^2\alpha_R^2 m_e l_d}{2\mu_B\mu_0 M_S e\hbar S_c}\left(\frac{1}{H_K} - \frac{H_E}{H_K(H_K + 2H_E)}\right) cos^2\varphi \#(S7)$$

By comparing the Eq. (S6) and Eq. (S7) with Eq. (5) in the manuscript, we could find that $L_{\eta_1 =- \eta_2}$ is larger than $L_{|\eta_1| \neq |\eta_2|}$ and much larger than $L_{\eta_1 = \eta_2}$ under the same material parameters, because the anisotropy field H_K is typically 1000 times smaller than the exchange coupling field H_E. By fixing $\eta_1 =+ 1$ and changing η_2 from -1 to +1, the results of low frequency inductance $\mathrm{L}_{f \ll f_{AFMR}}$ under different η_2 are shown in Fig. S2. $\mathrm{L}_{f \ll f_{AFMR}}$ reaches its maximum when $\eta_2 =- 1$(opposite sublattice SOC configuration), and decays monotonically by nearly 75% when η_2 is increased to 0 (asymmetric sublattice SOC), and keep the trend of decreasing and finally reaches its minimum when $\eta_2 =+ 1$ (identical sublattice SOC configuration).

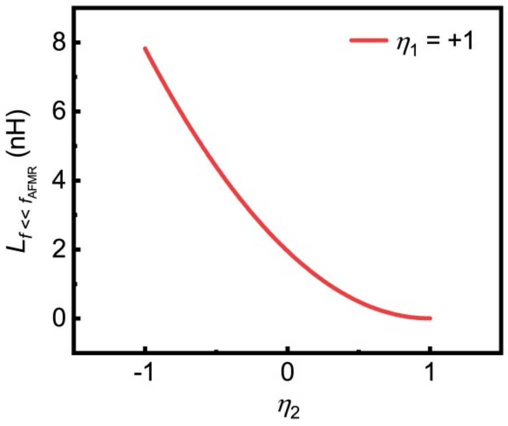

FIG. S2. Low frequency emergent inductance when $f \ll f_{AFMR}$ under different values of η_2 from -1 to +1 with fixed $\eta_1 = +1$.

Supplementary Note 5: Physical explanation of the critical role of opposite sublattice SOC to the generation of emergent inductance

As shown in Fig. S2, the emergent inductance at low frequency region obtains maximum under the configuration of $\eta_1 = -\eta_2$, which stressed out the importance of opposite SOC configuration to the generation of emergent inductance. The physics behind this can be explained by detailed analysis of SOT-induced sublattice magnetization dynamics and the form of spin motive force under different SOC configuration. Under the condition of alternating electric current injection $j_{e,\omega} = j_e e^{i\omega t}$ along *x* axis with low frequency $f = \frac{\omega}{2\pi} \ll f_{AFMR}$ and small current density j_e, the sublattice magnetization could be assumed to follow instantaneous effective field $H_{eff,i}(t)$ adiabatically, remaining in a state of local equilibrium at every point throughout the alternating cycle. By further assuming the electric current is injected along +***x*** direction, $H_{eff,i}(t)$ could be analytically written as below after reviewing the coupled LLG equation Eq. (3) in the manuscript:

$$H_{eff,i}(t) = -2H_E m(t) + H_K m_{i,x}(t)x + H_{SOC,i}(t)y \#(S8)$$

where SOC effective field $H_{SOC,i}(t)$ is proportional to $\eta_i j_e e^{i\omega t}$, $m_{i,x}(t) \approx +1(-1)$ for sublattice 1(2) which means that magnetic anisotropy field H_K term maintains nearly unchanged, and the antiferromagnetic exchange coupling field H_E is typically 1000 times larger than H_K and $H_{SOC,i}$ in magnitude.

In the following we will discuss the low frequency SOT-induced sublattice magnetization precession under three different SOC configurations: identical sublattice SOC with $\eta_1 = \eta_2 = +1$, opposite sublattice SOC with $\eta_1 = -\eta_2 = +1$ and asymmetric sublattice SOC ($\eta_1 = +1$, $\eta_2 = 0$).

A. In the first scenario, sublattice magnetization m_1 and m_2 undergo coherent canting toward the +*y* direction as the *y* component of $H_{eff,i}(t)$, $H_{SOC,i}(t)$, increases. This contributes to an accumulation of net magnetization m and further activates H_E term, which is along -*y* direction, opposes the driving force $H_{SOC,i}(t)$ term, and effectively confines the increasing of the *y* component of $H_{eff,i}(t)$. The limited sublattice magnetization motion throughout one alternating cycle finally leads to a weak, coherent precession, as shown in Fig. S3(a).

B. Conversely, in the second scenario, since the *y* component of $H_{eff,i}(t)$, $H_{SOC,i}(t)$, is opposite to each other in the two sublattices, m_1 and m_2 exhibit anti-parallel staggered canting following the change of $H_{eff,i}(t)$ along the +*y* and -*y* direction respectively, characterized by an increasing Néel vector n and vanishing m. The absence of net magnetization effectively quenches H_E term, allowing for an uncompensated $H_{SOC,i}(t)$ which determines the motion of sublattice magnetization independently. A large-amplitude staggered precession is induced accordingly, as shown in Fig. S3(b).

C. The third scenario represents an intermediate case where $H_{SOC,i}(t)$ acts exclusively on m_1. Initially, by following the change of $H_{SOC,i}(t)$, the resulting motion of m_1 induces a finite m, which is weaker than the counterpart in the first scenario, because only one sublattice magnetization is activated. The generation of m simultaneously triggers H_E term to suppress the *y* component of $H_{eff,1}(t)$ and activate the *y* component of $H_{eff,2}(t)$, resulting in compensated growth of m_1 along +*y* direction and promoted growth of m_2 along -*y* direction. Note that a stronger motion of m_1 than m_2 is required to sustain the existence of m. Finally, this results in a non-equal staggered precession with an intermediate amplitude, bounded by the limits of the first and second scenarios, as shown in Fig. S3(c).

In summary, the main difference between identical, opposite and asymmetric sublattice SOC configuration is regarding the contribution from H_E, which is present and suppresses total magnetization precession in the first and last situation, while nearly absent and does not influence precession process in the second situation.

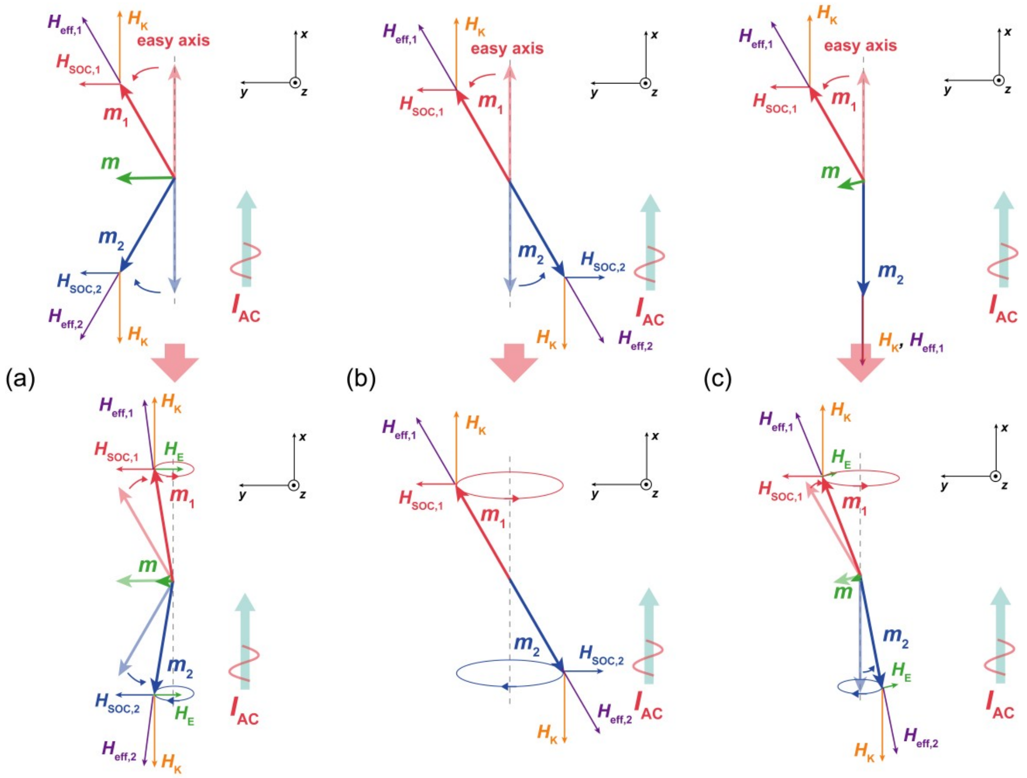

FIG. S3. SOT-induced sublattice magnetization precession analysis based on adiabatical assumption of effective field tracking under low frequency, small amplitude alternating electric current injection condition in identical sublattice SOC situation with $\eta_1 = \eta_2 = +1$ (a), opposite sublattice SOC situation with $\eta_1 = -\eta_2 = +1$ (b) and asymmetric sublattice SOC situation with $\eta_1 = +1$, $\eta_2 = 0$ (c). The top panel shows the initial stage of sublattice magnetization motion when $H_{SOC,i}(t)$ term is switched on, while the bottom panel shows the further motion of sublattice magnetization depending on whether H_E term is activated and the anticipated precession trajectories throughout one alternating cycle.

Our illustrative analysis is further verified by macro-spin simulations with $j_e = 1MA/cm^2$ and $f = 1\,GHz$. The simulation results are shown in Fig. S4. For the situation of identical sublattice SOC configuration, both the precession of net magnetization m and Néel vector n is weak as shown in Fig. S4(a) and Fig. S4(c). While for the situation of opposite sublattice SOC configuration, the precession of net magnetization m is nearly absent while the precession of Néel vector n is strong and obvious, as shown in Fig. S4(b) and Fig. S4(d). In the case of asymmetric sublattice

SOC, the precession amplitudes of Néel vector n and net magnetization m are approximately halved relative to the opposite and identical sublattice SOC configurations respectively, as shown in Fig. S4(c) and Fig. S4(e). Especially, it is the spin precession along the y axis that directly contributes to the SMF, as discussed in the following, thus eventually resulting in a considerable inductance when the SOC in each sublattice is opposite.

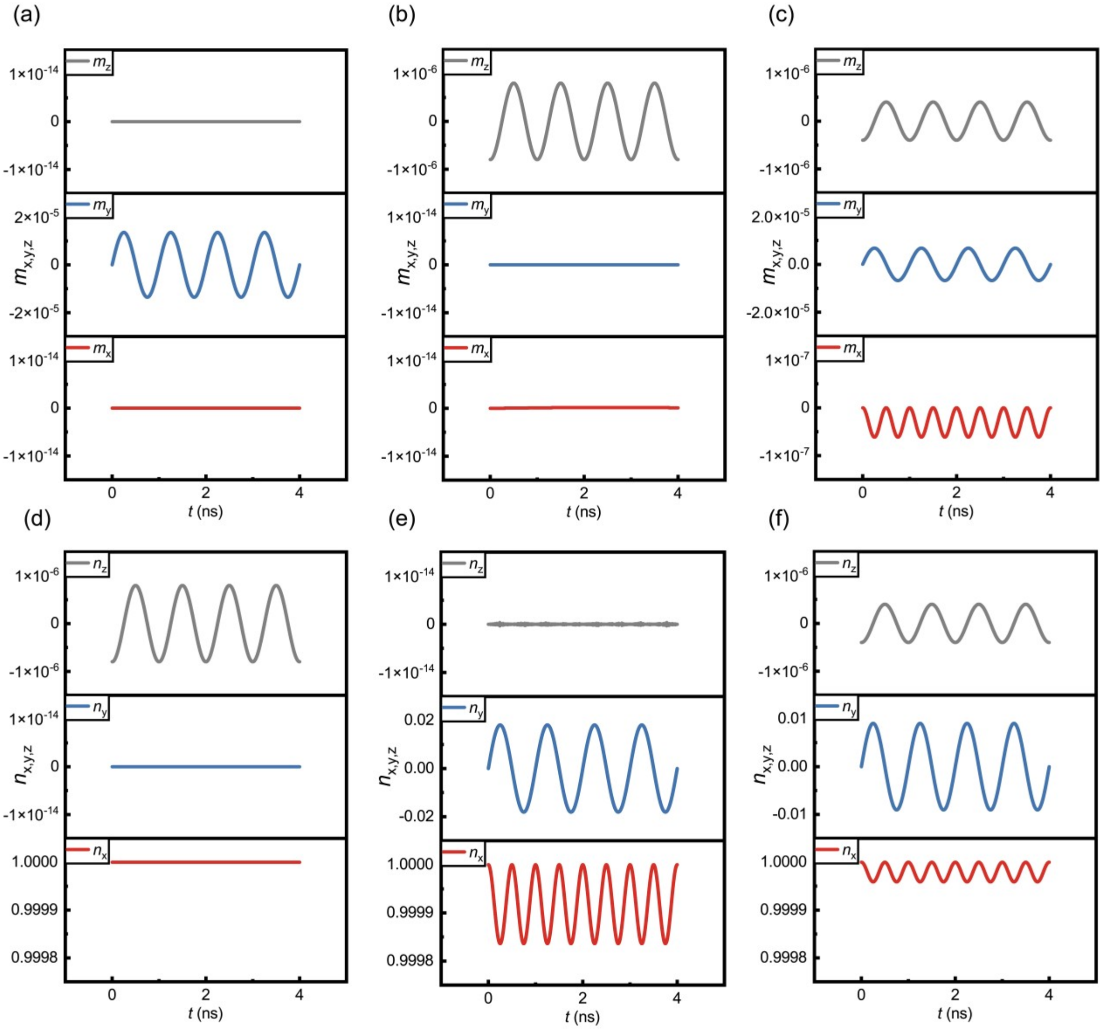

FIG. S4. Macro-magnetic simulation of SOT-induced Néel vector n and net magnetization m precession analysis under identical sublattice SOC with $\eta_1 = \eta_2 =+1$ ((a) and (c)), opposite sublattice SOC with $\eta_1 =- \eta_2 =+1$ ((b) and (d)) and asymmetric sublattice SOC with $\eta_1 =+1$ while $\eta_2 = 0$ ((c) and (e)). $j_e = 1\ MA/cm^2$ and $f = 1\ GHz$ is absorbed, and other material parameters follow the identical value demonstrated in TABLE I in the manuscript.

In the manuscript, the spin motive force ε_{SMF} is defined by Eq. (2) after integrating the spin electric field $E_{\pm}$ along the device's long axis, which coincide with the current injection axis and magnetic anisotropy axis (namely ***x*** axis) here. The angle φ in Eq. (2) is therefore zero and the ε_{SMF} becomes:

$$\varepsilon_{SMF} = -\frac{P\alpha_R m_e l_d}{2e\hbar}\sum_i \eta_i \frac{\partial m_{i,y}}{\partial t} \#(S9)$$

For identical sublattice SOC configuration ($\eta_1 = \eta_2 = +1$), Eq. (S9) reduces to:

$$\varepsilon_{SMF} = -\frac{P\alpha_R m_e l_d}{e\hbar}\frac{\partial m_y}{\partial t} \#(S10)$$

where m_y is the y component of net magnetization m. Since the magnitude for SOT-induced precession of m_y is largely compensated by antiferromagnetic exchange coupling field, the ε_{SMF} and thus emergent inductance is weak.

For opposite sublattice SOC configuration ($\eta_1 = -\eta_2 = +1$), Eq. (S9) reduces to:

$$\varepsilon_{SMF} = -\frac{P\alpha_R m_e l_d}{e\hbar}\frac{\partial n_y}{\partial t} \#(S11)$$

where n_y is the y component of the Néel vector n. Since the SOT-induced precession of n_y is not compensated by antiferromagnetic exchange coupling field and completely activated by SOT, the ε_{SMF} and thus emergent inductance is thus strong and obvious.

For asymmetric sublattice SOC configuration ($\eta_1 = +1$ while $\eta_2 = 0$), Eq. (S9) reduces to:

$$\varepsilon_{SMF} = -\frac{P\alpha_R m_e l_d}{2e\hbar}\left(\frac{\partial n_y}{\partial t} + \frac{\partial m_y}{\partial t}\right) \#(S12)$$

Since the SOT-induced precession of n_y is dominated compared the precession of m_y and partly compensated by antiferromagnetic exchange field, the ε_{SMF} and thus emergent inductance is thus intermediate between the counterpart in identical and opposite sublattice SOC configurations.

Supplementary Note 6: Planar Hall effect-like behaviour for the inductive signal along the device's transversal direction

The emergent inductance induced by spin motive force along the longitudinal direction of the prototype device shows a $cos^2\varphi$ relationship with the angle φ between the equilibrium orientation of Néel vector and the current injection direction. This angle-dependent behavior closely resembles the anisotropic magnetoresistance (AMR) observed in most AFM devices[16,17]. Interestingly, if we focus on the emergent electric field along device's transversal direction, the formula of spin motive force could be rewritten as:

$$\varepsilon_{SMF,transverse} = \frac{P\alpha_R m_e w_d}{2e\hbar}\sum_i \eta_i\left(\frac{\partial m_{i,x}}{\partial t}cos\varphi + \frac{\partial m_{i,y}}{\partial t}sin\varphi\right)\#(S13)$$

where w_d denotes device's width. By absorbing small-cone-precession assumption of SOT-motivated AFM dynamics under alternating electric current injection and opposite sublattice SOC configuration ($\eta_1 = -\eta_2$) for our candidate material Mn$_2$Au, Eq. (S13) could be further written as below according to Eq. (S2):

$$\varepsilon_{SMF,transverse} = -\frac{P^2\alpha_R^2 m_e w_d j_\omega \gamma\left(\gamma\mu_0(2H_E + H_K)i\omega - \alpha\omega^2\right)sin\varphi cos\varphi}{e\hbar\mu_B M_S \quad \omega^2 - \omega_{AFMR}^2 - 2i\Delta\omega}e^{i\omega t}\#(S14)$$

Finally, a Hall inductance along device's transversal direction could be obtained by $\mathcal{L} = -\frac{\varepsilon_{SMF}}{dI/dt}$:

$$\begin{cases} Re(\mathcal{L}_{transverse}) = -\dfrac{P^2\alpha_R^2 m_e \ \gamma^2\mu_0(2H_E + H_K)\left(\omega_{AFMR}^2 - \omega^2\right)}{\mu_B M_S e\hbar t_d \ \ (\omega_{AFMR}^2 - \omega^2)^2 + 4\Delta^2\omega^2}sin\varphi cos\varphi \\ Im(\mathcal{L}_{transverse}) = \dfrac{P^2\alpha_R^2 m_e \ \gamma\alpha\omega[\omega^2 + \gamma^2\mu_0^2(2H_E + H_K)^2]}{\mu_B M_S e\hbar t_d \ \ (\omega_{AFMR}^2 - \omega^2)^2 + 4\Delta^2\omega^2}sin\varphi cos\varphi \end{cases}\#(S15)$$

According to Eq. (S15), the Hall inductance shows a $sin\varphi cos\varphi$ relationship, which is analogous to the planar Hall effect (PHE) in AFM devices[18,19], as shown in Fig. S5. Different from the scaling law of longitudinal emergent inductance, the transversal inductance is merely inverse proportional to device's thickness since $\frac{w_d}{S_c} = \frac{1}{t_d}$. This explains why the magnitude of low frequency hall inductance of 39 pH is two orders lower than the longitudinal inductance shown in the manuscript, which is typically 7.82 nH. From the perspective of experimental measurement in the future, the observation of Hall inductance could be served as another important proof of emergent inductance phenomena in AFM systems beyond the observation of longitudinal inductance. Besides, it will provide a perspective to revisit the Hall signal regarding ultra-fast AFM dynamics, where the Hall resistance contributions, such as anomalous Hall effect (AHE), are mainly considered before.[8,20]

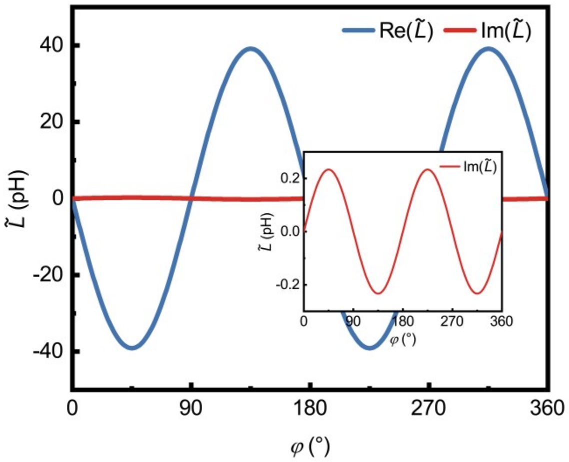

FIG. S5. The angular dependence of $Re(\tilde{L})$ (blue curve) and $Im(\tilde{L})$ (red curve) of emergent inductance along device's transversal direction at $f = 10\ GHz$.

Supplementary Note 7: Details of macrospin simulation for AFM dynamics

Macrospin simulations are performed to solve the spin dynamics of each sublattice numerically. All the simulations were performed at $T = 0$ K and no thermal effect was considered in this work. The simulation results were substituted into the Eq. (2) to calculate the SMF and the complex inductance among a wide range of parameters. The accuracy of Eq. (4) and Eq. (7) can be verified by checking the difference between simulations and formulas. Besides, we further incorporate non-zero external magnetic field into LLG equation during the macrospin simulation, to study the potential of magnetic-field immunity of the AFM emergent inductor compared with the counterpart based on other systems, such as FM/HM heterostructures. In that case, the magnetic energy density is written by:

$$u = A_0 m^2 - K\left(n_x^2 + m_x^2\right) - 2\mu_0 M_S m \cdot H \#(S16)$$

where the last term is incorporated to characterize the energy contribution from external magnetic field H.

In our macrospin simulations, the LLG equation follows Eq. (3) rather than single dynamical equation of Néel vector[21], which typically ignores any inter-sublattice spin dynamics due to the assumption of strictly antiparallel arrangement between m_1 and m_2. Micromagnetic or atomic simulations will offer more information about inter-sublattice dynamics, especially when the system is stimulated by ultrafast SOT. However, previous simulations of magnetization switching have demonstrated that the averaged spin dynamics obtained from atomic-scale simulations reproduce basically the results derived from macrospin simulations.[22] We thus believe that our macrospin simulations could be used to verify the accuracy of the derived formulas, especially taking into account the small cone-angle precession.

Supplementary Note 8: Formula derivation of first-order approximation of nonlinear inductance

As defined in the manuscript, only the deterioration of $m_{i,0}$ and its influence on the precession of $m_{i,y}$ and $m_{i,z}$ at fundamental frequency f are taken into account for first-order approximation of emergent inductance in nonlinear region. In this case, The assumption of $m_i \simeq m_{i,0}\hat{x} + e^{i\omega t}(\tilde{m}_{i,\omega}^{y}\hat{y} + \tilde{m}_{i,\omega}^{z}\hat{z})$ with $m_{1,0} =- m_{2,0}$is still valid, while the only difference from small-cone-angle assumption is that $|m_{i,0}|$ could not be approximated by unity. By substituting this assumption and opposite sublattice SOC configuration ($\eta_1 =- \eta_2 =- 1$) into Eq. (3), we could obtain new formulas for $\tilde{m}_{i,\omega}^{y}$ and $\tilde{m}_{i,\omega}^{z}$:

$$\begin{cases} \tilde{m}_{1,\omega}^{y} = \dfrac{P\alpha_R j_\omega m_{1,0}^2 - \gamma(2\gamma\mu_0 H_E + \gamma\mu_0 H_K + \alpha i\omega)}{\mu_B M_S \quad \omega^2 - m_{1,0}^2\omega_{AFMR}^2 - 2m_{1,0}^2 i\Delta\omega} \\ \tilde{m}_{2,\omega}^{y} = \dfrac{P\alpha_R j_\omega m_{1,0}^2\,\gamma(2\gamma\mu_0 H_E + \gamma\mu_0 H_K + \alpha i\omega)}{\mu_B M_S \quad \omega^2 - m_{1,0}^2\omega_{AFMR}^2 - 2m_{1,0}^2 i\Delta\omega} \\ \tilde{m}_{1,\omega}^{z} = \dfrac{P\alpha_R j_\omega m_{1,0} \qquad \gamma i\omega}{\mu_B M_S \quad \omega^2 - m_{1,0}^2\omega_{AFMR}^2 - 2m_{1,0}^2 i\Delta\omega} \\ \tilde{m}_{2,\omega}^{z} = \dfrac{P\alpha_R j_\omega m_{1,0} \qquad \gamma i\omega}{\mu_B M_S \quad \omega^2 - m_{1,0}^2\omega_{AFMR}^2 - 2m_{1,0}^2 i\Delta\omega} \end{cases} \#(S17)$$

By adapting the critical constraint $|m_i|^2 \equiv 1$, $m_{i,0}$ could be computed by:

$$m_{i,0}^2 + \frac{1}{2}(|\tilde{m}_{i,\omega}^{y}|^2 + |\tilde{m}_{i,\omega}^{z}|^2) = 1\#(S18)$$

The analytical solution of Eq. (S17) and Eq. (S18) are too complicated to demonstrate. We thus choose to obtain $m_{i,0}$ numerically after substituting all the parameter values. The spin motive force ε_{SMF} could be thus derived from Eq. (2):

$$\varepsilon_{SMF} = \frac{P^2\alpha_R^2 m_e l_d j_\omega m_{1,0}^2\gamma(\gamma\mu_0(2H_E + H_K)i\omega - \alpha\omega^2)}{2e\hbar\mu_B M_S \quad \omega^2 - m_{1,0}^2\omega_{AFMR}^2 - 2im_{1,0}^2\Delta\omega} cos^2\varphi e^{i\omega t}\#(S19)$$

Supplementary Note 9: Fitting robustness of first-order approximation under different material parameters and fixed frequency

We further compare the $Re(\tilde{L})$ predicted by linear inductance model (Eq. (4)), first-order approximation (Eq. (6)) with numerical simulation results at a relatively high fixed operating frequency $f = 100\,GHz$ but different current density and material parameters, including H_K, H_E and α. As shown in Fig. S6, Eq. (6) generally shows better fitting results than Eq. (4) under different configuration of H_E and α, while it overestimates the magnitude changing of $Re(\tilde{L})$ within the region of small H_K. This is reasonable since the changing of H_E and α mainly influences the magnetization precession behaviour in the vicinity of f_{AFMR} and $f < f_{AFMR}$ is always maintained. In contrast, the decreasing of H_K will make the activation of sublattice magnetization precession in the low frequency region much easier under a small current injection, resembling the situation of unchanged H_K but larger current injection approaching and even exceeding $J_{e,th}$. In that way, the nonlinear behaviour of sublattice magnetization dynamics, which incorporates the unavoidable contributions from the emergence of higher harmonics, can not be predicted well by first-order approximation merely considering the changing of $m_{i,0}$.

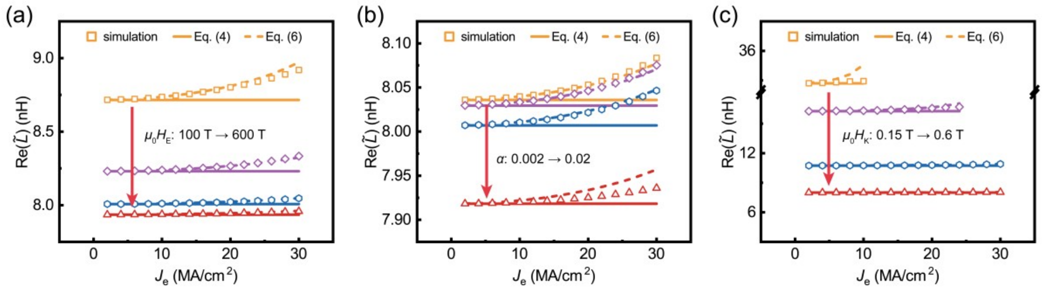

FIG. S6. Comparison of Eq. (4) and Eq. (6) with numerical simulation results under different material parameters H_E (a), α (b) and H_K (c). $\mu_0 H_\mathrm{E}$ is selected to be 100 T, 200 T, 400 T, 600 T with $\mu_0 H_\mathrm{K}$=0.6 T and α=0.01 in (a), α is selected to be 0.002, 0.005, 0.01, 0.02 with $\mu_0 H_\mathrm{E}$=400 T and $\mu_0 H_\mathrm{K}$=0.6 T in (b), $\mu_0 H_\mathrm{K}$ is choose to be 0.15 T, 0.3 T, 0.45 T, 0.6 T with $\mu_0 H_\mathrm{E}$=400 T and α=0.01 in (c). f is fixed to 100 GHz for all the situations.

Supplementary Note 10: Quantitative scaling law of $J_{e,th}$ under different frequency and material parameters

By using Eq. (6) to estimate $Re(\tilde{L}_{sim})$ and $A_{m_{i,y}, sim}$, a quantitative scaling law between $J_{e,th}$ and frequency and material parameters could be obtained, as shown in Figs. S7. Firstly, as predicted, $J_{e,th}$ will decay with the increasing of operating frequency f, as shown in Fig. S7(a). Secondly, as shown in Fig. S7(b) and (c), $J_{e,th}$ exhibits a relationship that is neary directly proportional to magnetic anisotropy field H_K and nearly unchanged with the increasing of Gilbert damping constant α. This is reasonable since larger H_K means larger f_{AFMR} and weaker sublattice magnetization precession behaviour at the same current injection and working frequency, which will boost $J_{e,th}$. While the increasing of α merely exert obvious influence on the sublattice magnetization precession in the frequency region near f_{AFMR}, which hardly influence the sublattice magnetization precession even at a relatively high frequency ($f = 100$ GHz). Lastly, as shown in Fig. S7(d), $J_{e,th}$ exhibits a logarithmic scaling behavior as a function of antiferromagnetic exchange coupling field. This is understandable since the increasing of H_E means the shift of f_{AFMR} towards higher frequency region and leads to weaker sublattice magnetization dynamics in low frequency. The improvement of $J_{e,th}$ is dramatic when H_E is small since the operating frequency is still in the vicinity of f_{AFMR}. While under large H_E, the increasing of $J_{e,th}$ will be slower gradually and finally approach saturation. Good fitting with numerical simulation results under wide range of frequency and material parameters as shown in Figs. S7, indicates that non-linear behaviour of our emergent inductance model can be mainly attributed to the equilibrium position drift of $m_{i,0}$, while the contribution from higher harmonics will only be obvious under large current injection in the vicinity of $J_{e,th}$ and cause signal distortion.

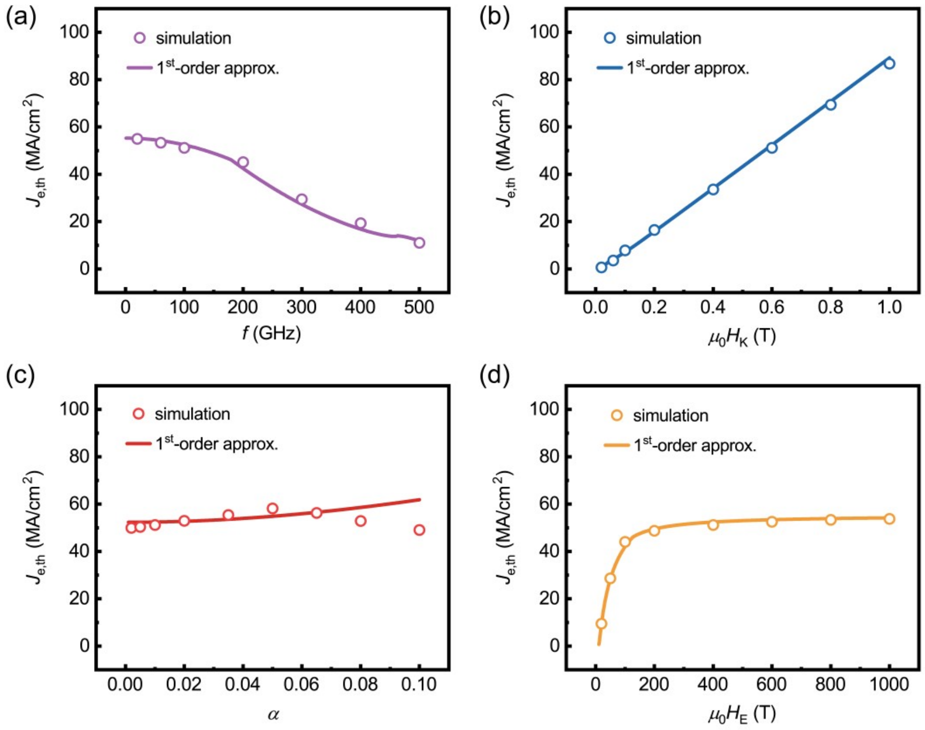

FIG. S7. Comparison of $J_{e,th}$ predicted by first-order nonlinear approximation (1st-order approx., solid line) with the results obtained from numerical simulations (open symbols) when f varies from 1 GHz to 500 GHz (a), when μ_0H_K varies from 0.02 T to 1 T (b), when α varies from 0.001 to 0.1, and when μ_0H_E varies from 11 T to 1000 T (d). For the $J_{e,th}$ estimation under different material parameters, f is fixed to 100 GHz.

Supplementary Note 11: Discussion of the emergence of higher harmonics terms and its impact on emergent inductance

The impact of higher harmonics on the magnetization dynamics of m_1 are analyzed by numerical simulation under relatively high current density $J_e = 40\ MA \cdot cm^{-2}$ (below threshold current density $J_{e,th} = 51.1\ MA \cdot cm^{-2}$) and $f = 100\ GHz$, as shown in Fig. S8. For the precession of $m_{1,y}$, the higher harmonics component is still negligible when compared with fundamental frequency component even under such a large J_e injection, which underscores the dominant place of first-order approximation among all the nonlinear terms. Generally, $m_{1,y}$ and $m_{1,z}$ components exhibit odd harmonics ($1\omega, 3\omega, 5\omega\ldots$) with gradually diminishing amplitudes and dominant position of basic frequency terms $m_{1,y,1\omega}$ and $m_{1,z,1\omega}$, whereas $m_{1,x}$ features even harmonics ($2\omega, 4\omega\ldots$) with a similar decaying trend and a considerable equilibrium position shift from unity.

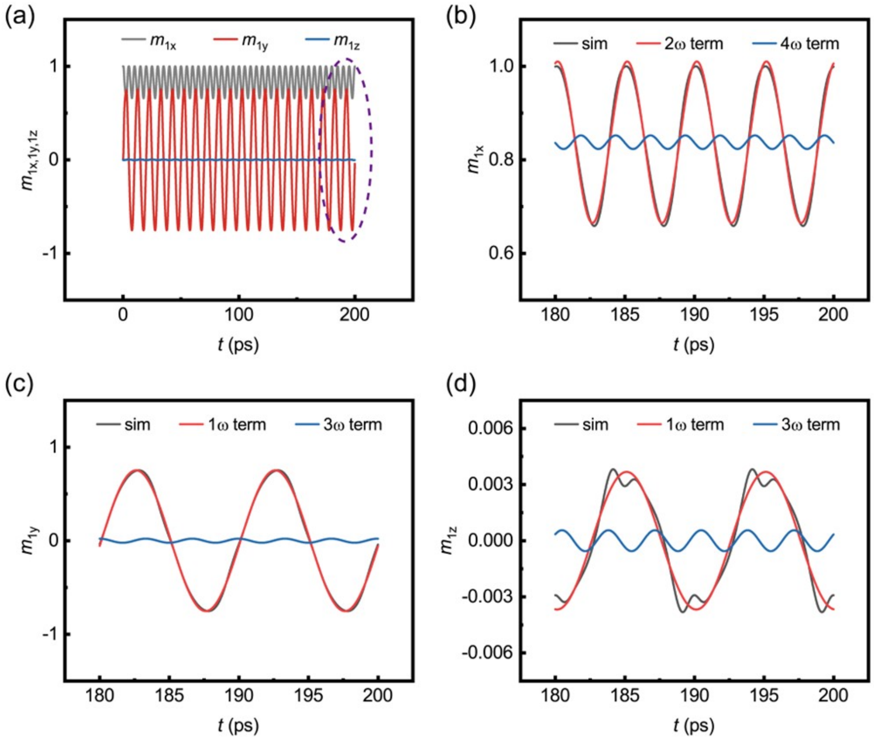

FIG. S8. (a) Macrospin simulations of m_x (black line), m_y (red line) and m_z (blue line) for sublattice 1 in Mn$_2$Au under $f = 100\ GHz$ and $J_e = 40\ MA \cdot cm^{-2}$. (b) the 2ω (red line) term and 4ω (blue line) term extracted from the fitting results of simulated trajectory m_{1x} (black line). (c) the 1ω (red line) term and 3ω (blue line) term extracted from the fitting results of simulated trajectory m_{1y} (black line). (d) the 1ω (red line) term and 3ω (blue line) term extracted from the fitting results of simulated trajectory m_{1z} (black line).

Similar to the evolution of the equilibrium position drift of $m_{i,0}$, higher-order harmonics become increasingly pronounced as J_e increases, which is further verified by the simulation results of amplitude ratio and phase difference between fundamental frequency term and higher harmonics term. As shown in Fig. S9(a), the amplitude of 3ω harmonics is typically two orders smaller than basic frequency term with a stable phase difference when J_e is low, while in the vicinity of $J_{e,th}$, the amplitude ratio will be boosted to nearly 10% accompanied by a 50% reduction of phase difference.

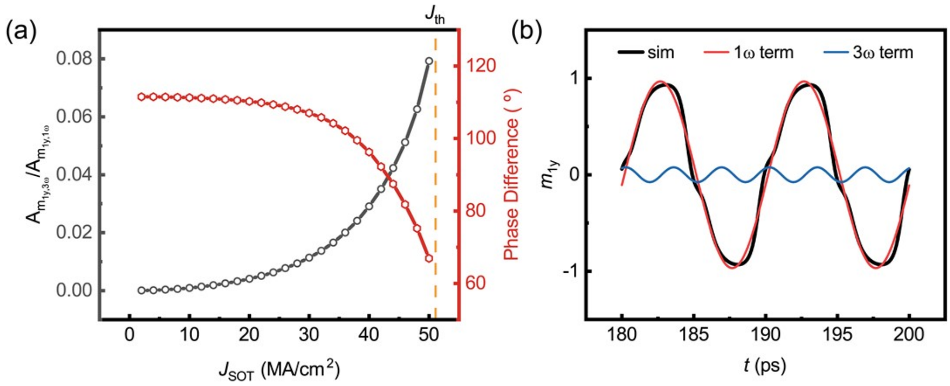

FIG. S9. (a) Amplitude ratio and phase difference between magnetization precession with 3ω harmonics and 1ω basic frequency for sublattice 1 under different current density obtained by numerical simulations. (b) Simulated trajectory of m_{1y} with the extracted 1ω and 3ω terms under a large current density $J_e = 50\ MA \cdot cm^{-2}$ close to $J_{e,th} = 51.1\ MA \cdot cm^{-2}$. f is fixed to 100 GHz for all the situations.

Finally, we discuss the impact of higher harmonics on the operation of our emergent inductance device. The existence of higher harmonics is harmful to the operation of an inductor device, which will potentially induce unwanted oscillation phenomena of parasitic inductance or capacitance and electromagnetic wave radiation at harmonic frequency. Besides, the phase shift between the fundamental 1ω signal and its harmonics can lead to waveform distortion, often manifesting as spikes near the zero crossings. This potential impact is further analyzed by the waveform simulation of $m_{i,y}$ under large external current close to $J_{e,th}$. As shown in Fig. S9(b), even though the shape of basic frequency precession is still maintained in this extreme current region, a small distortion appears near the zero crossing points since the amplitude of higher harmonics could not be ignored easily in this situation. In the realistic application in the future, the emergent inductor device should avoid operating at current density close or above $J_{e,th}$ besides working within the bandwidth determined by f_{AFMR}. And a more precise definition of $J_{e,th}$ will be required depending on the tolerance degree of signal distortion and oscillation condition of external parasitic circuits under higher harmonic frequency.

Interestingly, the nonlinear effect and the emergence of higher harmonic inductance contributed from spin-transfer torque (STT)-motivated spin motive force in spiral magnet-based inductor and AFM DW-based inductor has been successfully observed in experiments and theoretically analyzed[23-28]. In future experiments, the observation of higher harmonic signal will serve as another important proof of our formula derivation beyond emergent inductance with basic harmonics, both of which are proportional to frequency and can be distinguished from harmonic signal contributed by magnetoresistance behaviour[29-31].

Supplementary Note 12: Comparison of the emergent inductance in SOC-FM systems and SOC-AFM systems under external magnetic field

Regardless of whether the emergent inductance originates from spiral magnet systems, non-AFM DW systems or SOC-FM systems (like FM/HM heterostructures), the magnetic moments in such devices tend to align along the direction of external magnetic field.[23-27,32-34] This alignment will significantly affect the magnetization precession induced by STT or SOT, thereby leading to a pronounced modification of the resulting inductance value. In contrast, in our SOC-AFM emergent inductor, the presence of antiferromagnetic exchange coupling field H_E effectively stabilizes the magnetic configuration. As a result, both the sublattice spin direction and the SOT-induced precession will be hardly influenced by external magnetic fields, giving rise to a certain degree of magnetic-field immunity in the inductance response.

Figs. S10 shows the simulation results of the real part of the low-frequency emergent inductance for SOC-AFM and SOC-FM systems under external magnetic fields of different directions and magnitudes. Here, the opposite sublattice SOC configuration with ($\eta_1 = -\eta_2$) is assumed for SOC-AFM system. The simulation details of emergent inductance in SOC-FM systems are described in Supplementary Note 13. Here, the electric current density is chosen as $1\,MA \cdot cm^{-2}$ to satisfy the assumption of small cone-angle precession, and the operating frequency is chosen as 1 GHz, which is below both the resonance frequencies of SOC-FM system (~10 GHz) and SOC-AFM system (sub-THz). We could find that the emergent inductance of the AFM inductor device remains nearly unchanged under 1 T magnetic field regardless of whether the direction is along *x*, *y* or *z* direction. However, the emergent inductance in devices based on SOC-FM system varies significantly due to the 90° switching of FM moment from easy axis (*z* axis) to *xoy* plane under external magnetic field along *x* or *y* direction, or 180° switching of FM moment between +*z* and -*z* direction under external magnetic field along *z* axis.

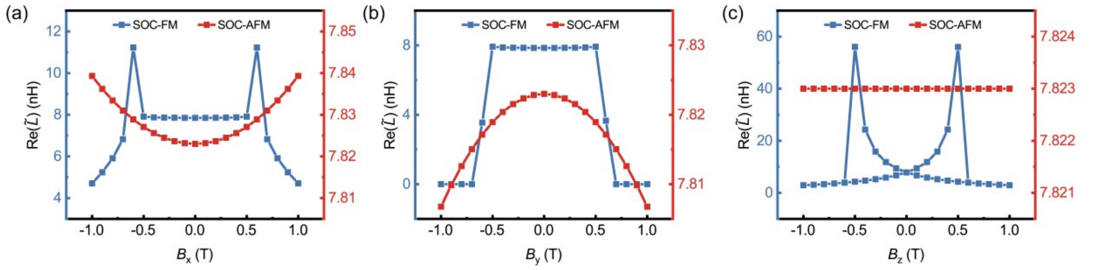

FIG. S10. The influence of magnetic field along *x* axis (a), *y* axis (b) and *z* axis (c) on the real part of the emergent inductance in SOC-FM systems (blue line, with *z* axis the magnetic anisotropy axis) and SOC-AFM systems (red line, with *x* axis the magnetic anisotropy axis).

Supplementary Note 13: Simulation details of emergent inductance under external magnetic field in SOC-FM systems

In typical SOC-FM systems like FM/HM heterostructures, the emergent inductance stems from the SOT-induced magnetization precession and SOC-related spin motive force $\varepsilon_{SMF,\,FM/HM}$, which could be expressed as below[35]:

$$\varepsilon_{SMF,\,FM/HM} =- \frac{P\alpha_{R,FM/HM} m_e l_d}{e\hbar} \frac{\partial m_y}{\partial t} \#(S20)$$

where $\alpha_{R,FM/HM}$ the Rashba constant describes the SOC strength at the FM/HM interface, and m_y is the component of FM magnetic moment m along *y* direction. Here the electric current is assumed to be injected along *x* axis. Within single-domain approximation with magnetic anisotropy along *z* direction (typical for FM/HM system), we assume the magnetic energy density depicted by:

$$u =- \mu_0 M_S m \cdot H - K m_z^2 \#(S21)$$

where the first term characterizes the energy contribution from external magnetic field H, and the second term denotes the uniaxial magnetic anisotropy energy. Considering the contribution from SOT, the dynamics of m can be depicted by following Landau-Lifshitz-Gilbert (LLG) equation:

$$\frac{\partial m}{\partial t} = \gamma m \times \frac{1}{M_S} \frac{\delta u}{\delta m} + \alpha m \times \frac{\partial m}{\partial t} - \gamma m \times \mu_0 H_{SOC} \#(S22)$$

where the effective field H_{SOC} of which can be written by[36]:

$$H_{SOC} = \frac{P\alpha_{R,FM/HM}}{\mu_0 \mu_B M_S} \left(\hat{z} \times J_e\right) \#(S23)$$

The macrospin simulation is further performed by combining Eqs. (S21) to (S23), and the emergent inductance could be calculated as below after obtaining the simulation results of m_y and then substituting it into Eq. (S20):

$$\tilde{L}_{FM/HM} =- \frac{\varepsilon_{SMF,\,FM/HM}}{dI/dt} \#(S24)$$

All the parameters adopted here are set identical to the values in Table I: Rashba constant $\alpha_{R,FM/HM} = 10^{-10}\, eV \cdot m$, spin polarization $P = 0.5$, saturation magnetization $M_S = 796\, kA \cdot m^{-1}$, magnetic anisotropy energy $K = 4.77 \times 10^5\, J \cdot m^{-3}$, sectional-area $S_c = 10^{-3}\, \mu m^2$ (with width 100 nm and thickness 10 nm), length of devices $l_d = 10\, \mu m$, damping constant $\alpha = 0.01$. In Fig. S10(a) and Fig. S10(b), the in-plane magnetic field is swept from +1 T to -1 T to obtain the results. In Fig. S10(c), the out of plane magnetic field is swept from +1 T to -1 T to obtain the results of SOC-AFM inductor while it is swept between +1 T and -1 T forward and backward to obtain the results of SOC-FM inductor.

Supplementary Note 14: Compatibility analysis of AFM emergent inductor with AFM memory technologies

As a novel branch of the device application of AFM family, our AFM emergent inductor shares common benefits with AFM memory device[37] in terms of size scalability[38], magnetic field immunity[38,39] and ultrafast operating frequency[40,41]. In fact, the memory and inductor functionalities are promising to be integrated within single device based on candidate material Mn$_2$Au, which has been proved to be a reliable AFM memory system[42]. From principle, the stable data storage and large inductance can be realized in AFM devices simultaneously, because they can be modulated by H_E and H_K respectively. In contrast, for SOC-FM based emergent inductors, although they can share a similar film stack with FM memory devices, integrating both memory and inductive functionalities within a single device is practically unfeasible. This is because robust information storage requires a large H_K, whereas maximizing inductance necessitates a small H_K.[43]

Here we demonstrate the operating mechanism of our memory-inductor-integrated prototype device. As shown in Fig. S11(a), the data is recorded by the orientation of Néel vector when the prototype device works as a memory device. The reading function can be realized by measuring AMR[42] between the two ends of Mn$_2$Au bottom electrode or Tunneling-AMR (TAMR)[44,45] through Mn$_2$Au/MgO/Pt heterojunction, while the writing process can be completed by SOT-induced 90° switching of Néel vector under the injection of pulsed current. As shown in Fig. S11(b), inductive behavior could be activated by SOT-induced magnetization precession under the injection of alternating current when the device works as an inductor device. The inductance signal will be captured by frequency-dependent voltage from spin-motive force between the two ends of the bottom electrode.

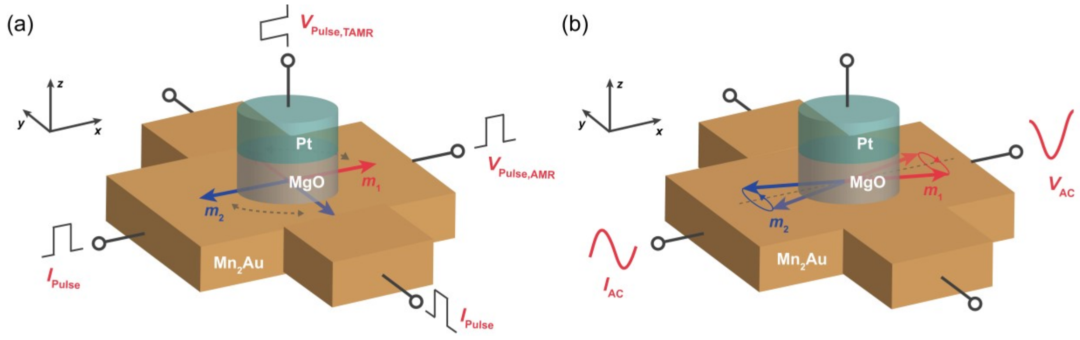

FIG. S11. Operating mechanism of memory-inductor-integrated prototype device based on single Mn_2Au electrode or Mn_2Au/MgO/Pt heterojunction when it works as memory functionality (a) or inductor functionality (b).

As we discussed in the part of 'Potentials and Challenges of AFM-based emergent inductor' in our original manuscript, the concept of emergent inductance could be further extended, and more candidate materials to construct inductor device can be discovered after detailed analysis. Recently, some emerging systems like non-colinear AFMs[46,47], and altermagnets[48,49] have become the research focus in the field of AFM memory, which shows spin-splitting energy band and large signal readout based on Tunneling Magnetoresistance (TMR) effect. It is promising to investigate emergent inductance in these systems and also the possibility of achieving both memory and inductor functionality in single device, which is out of the scope of this work and deserves further exploration in the future.

References

1. R. Cheng, J. Xiao, Q. Niu, and A. Brataas, *Phys. Rev. Lett.*, 2014, **113**, 057601.
2. A. Kanj, S. Mantion, I. Boventer, P. Bortolotti, V. Cros, A. Anane, O. Gomonay, and R. Lebrun, *Phys. Rev. Lett.*, 2025, **135**, 156703.
3. L. Huang, Y. Cao, H. Qiu, H. Bai, L. Liao, C. Chen, L. Han, F. Pan, B. Jin, and C. Song, *Nat. Commun.*, 2024, **15**, 7227.
4. R. Sepehrinia, S. Eskandari, and A. Qaiumzade, *Phys. Rev. B*, 2024, **110**, 014440.
5. P. Vaidya, S. Morley, J. Tol, Y. Liu, R. Cheng, A. Brataas, D. Lederman, and E. Barco, *Science*, 2020, **368**,160-165.
6. R. Cheng, D. Xiao, and A. Brataas, *Phys. Rev. Lett.*, 2016, **116**, 207603.
7. R. Khymyn, I. Lisenkov, V. Tiberkevich, B. Ivanov, and A. Slavin, *Sci. Rep.*, 2017, **7**, 43705.
8. Y. Takeuchi, Y. Yamane, J. Yoon, R. Itoh, B. Jinnai, S. Kanai, J. Ieda, S. Fukami, and H. Ohno, *Nat. Mater.*, 2021, **20**, 1364-1370.
9. J. Han, P. Zhang, Z. Bi, Y. Fan, T. Safi, J. Xiang, J. Finley, L. Fu, R. Cheng, and L. Liu, *Nat. Nanotechnol.*, 2020, **15**, 563-568.
10. A. Kanj, O. Gomonay, I. Boventer, P. Bortolotti, V. Cros, A. Anane, and R. Lebrun, *Sci. Adv.*, 2023, **9**, eadh1601.
11. J. Železný, H. Gao, K. Výborný, J. Zemen, J. Mašek, A. Manchon, J. Wunderlich, J. Sinova, and T. Jungwirth, *Phys. Rev. Lett.*, 2014, **113**, 157201.
12. J. Železný, H. Gao, A. Manchon, F. Freimuth, Y. Mokrousov, J. Zemen, J. Mašek, J. Sinova, and T. Jungwirth, *Phys. Rev. B*, 2017, **95**, 014403.
13. J. Sklenar, W. Zhang, M. Jungfleisch, W. Jiang, H. Saglam, J. Pearson, J. Ketterson, and A. Hoffmann, *AIP Adv.*, 2016, **6**, 055603.
14. T. Suzuki, S. Fukami, N. Ishiwata, M. Yamanouchi, S. Ikeda, N. Kasai, and H. Ohno, *Appl. Phys. Lett.*, 2011, **98**, 142505.
15. S. Zhang, Z. Wang, B. Li, W. Lu, M. Tian, Y. Sun, H. Du, and D. Shao, *Phys. Rev. Lett.*, 2026, **136**, 096702.
16. D. Kriegner, K. Výborný, K. Olejník, H. Reichlová, V. Novák, X. Marti, J. Gazquez, V. Saidl, P. Němec, V. Volobuev, G. Springholz, V. Holý, and T. Jungwirth, *Nat. Commun.*, 2016, **7**, 11623.
17. S. Bodnar, L. Šmejkal, I. Turek, T. Jungwirth, O. Gomonay, J. Sinova, A. Sapozhnik, H. Elmers, M. Kläui, and M. Jourdan, Nat. Commun., 2018, **9**, 348.
18. X. Zhou, J. Zhang, F. Li, X. Chen, G. Shi, Y. Tan, Y. Gu, M. Saleem, H. Wu, F. Pan, and C. Song, *Phys. Rev. Applied*, 2018, **9**, 054028.
19. G. Yin, J. Yu, Y. Liu, R. Lake, J. Zang, and K. Wang, *Phys. Rev. Lett.*, 2019, **122**, 106602.
20. L. Šmejkal, A. MacDonald, J. Sinova, S. Nakatsuji, and T. Jungwirth, *Nat. Rev. Mater.*, **7**, 2022, 482-496.
21. X. Chen, R. Zarzuela, J. Zhang, C. Song, X. Zhou, G. Shi, F. Li, H. Zhou, and W. Jiang, *Phys. Rev. Lett.*, 2018, **120**, 207204.
22. P. Roy, R. Otxoa, and J. Wunderlich, *Phys. Rev. B*, 2016, **94**, 014439.
23. T. Yokouchi, F. Kagawa, M. Hirschberger, Y. Otani, N. Nagaosa, and Y. Tokura,

Nature (London), 2020, **586**, 232.

24. A. Kitaori, N. Kanazawa, T. Yokouchi, F. Kagawa, N. Nagaosa, and Y. Tokura, *Proc. Natl. Acad. Sci. U.S.A.*,2021, **118**, e2105422118.
25. D. Kurebayashi and N. Nagaosa, *Commun. Phys.*, 2021, **4**, 260.
26. A. Kitaori, J. White, N. Kanazawa, V. Ukleev, D. Singh, Y. Furukawa, T. Arima, N. Nagaosa, and Y. Tokura, *Phys. Rev. B*, 2023, **107**, 024406.
27. T. Yokouchi, Y. Yamane, Y. Araki, J. Ieda, and Y. Shiomi, arXiv, 2023, preprint, arXiv: 2312. 01553, https://arxiv.org/abs/2312.01553v1.
28. A. Kitaori, J. White, V. Ukleev, L. Peng, K. Nakajima, N. Kanazawa, X. Yu, Y. Ōnuki, and Y. Tokura, *Commun. Phys.*, 2024, **7**, 159.
29. J. Godinho, H. Reichlová, D. Kriegner, V. Novák, K. Olejník, Z. Kašpar, Z. Šobáň, P. Wadley, R. Campion, R. Otxoa, P. Roy, J. Železný, T. Jungwirth, and J. Wunderlich, *Nat. Commun.*, 2018, **9**, 4686.
30. S. Shim, M. Mehraeen, J. Sklenar, J. Oh, J. Gibbons, H. Saglam, A. Hoffmann, S. S. L. Zhang, and N. Mason, *Phys. Rev. X*, 2022, **12**, 021069.
31. D. Kim, K. Kim, K. Lee, J. Oh, X. Chen, S. Yang, Y. Pu, Y. Liu, F. Hu, P. Van, J. Jeong, K. Lee, and H. Yang, *Nat. Mater.*, 2024, **23**, 1509-1514.
32. Y. Matsushima, Z. Zhang, Y. Ohashi, T. Hatakeyama, G. Xiao, T. Funato, M. Matsuo, and H. Kaiju, *Appl. Phys. Lett.*,2024, **124**, 022404.
33. Z. Zhang, Y. Matsushima, Y. Shibata, T. Hatakeyama, M. Matsuzaka, T. Funato, M. Matsuo, and H. Kaiju, *J. Magn. Magn. Mater.*, 2024, **610**, 172500.
34. R. Yamada, D, Kurebayashi, Y. Fujishiro, S. Okumura, D. Nakamura, F. Yasin, T. Nakajima, T. Yokouchi, A. Kikkawa, Y. Taguchi, Y. Tokura, O. Tretiakov, and M. Hirschberger, *Nat. Phys.*, 2026, **22**, 239-244.
35. Y. Yamane and J. Ieda, *J. Magn. Magn. Mater.*, 2019, **491**, 165550.
36. I. Miron, G. Gaudin, S. Auffret, Be. Rodmacq, A. Schuhl, S. Pizzini, J. Vogel, and P. Gambardella, *Nat. Mater.*, 2010, **9**, 230.
37. C. Marrows, *Science*, 2016, **351**, 558-559.
38. A. Du, D. Zhu, K. Cao, Z. Zhang, Z. Guo, K. Shi, D. Xiong, R. Xiao, W. Cai, J. Yin, S. Lu, C. Zhang, Y. Zhang, S. Luo, A. Fert, and W. Zhao, *Nat. Electron.*, 2023, **6**, 425-433.
39. H. Yan, H. Mao, P. Qin, J. Wang, H. Liang, X. Zhou, X. Wang, H. Chen, Z. Meng, L. Liu, G. Zhao, Z. Duan, Z. Zhu, B. Fang, Z. Zeng, A. Bettiol, Q. Zhang, P. Tang, C. Jiang, and Z. Liu, *Nat. Commun.*, 2024, **15**, 4978.
40. K. Olejník, V. Schuler, X. Marti, V. Novάk, Z. Kašpar, P. Wadley, R. Campion, K. Edmonds, B. Gallagher, J. Garces, M. Baumgartner, P. Gambardella, and T. Jungwirth, *Nat. Commun.*, 2017, **8**, 15434.
41. K. Olejník, T. Seifert, Z. Kašpar, V. Novák, P. Wadley, R. Campion, M. Baumgartner, P. Gambardella, P. Němec, J. Wunderlich, J. Sinova, P. Kužel, M. Müller, T. Kampfrath, and T. Jungwirth, *Sci. Adv.*, 2018, **4**, eaar3566.
42. S. Reimers, Y. Lytvynenko, Y. Niu, E. Golias, B. Sarpi, L. Veiga, T. Denneulin, A. Kovάcs, R. Borkowski, J. Bläßer, M. Kläui, and M. Jourdan, *Nat.*

Commun., 2023, **14**, 1861.

43. Y. Yamane, S. Fukami, and J. Ieda, *Phys. Rev. Lett.*, 2022, **128**, 147201.
44. B. Park, J. Wunderlich, X. Martí, V. Holý, Y. Kurosaki, M. Yamada, H. Yamamoto, A. Nishide, J. Hayakawa, H. Takahashi, A. B. Shick, and T. Jungwirth, *Nat. Mater.*, 2011, **10**, 347-351.
45. V. Barthem, C. Colin, H. Mayaffre, M. Julien, and D. Givord, *Nat. Commun.*, 2013, **4**, 2892.
46. X. Wang, H. Yan, X. Zhou, H. Chen, Z. Feng, P. Qin, Z. Meng, L. Liu, and Z. Liu, *Materials Today Physics*, 2022, **28**, 100878.
47. B. Rimmler, B. Pal, and S. Parkin, *Nat. Rev. Mater.*, 2025, **10**, 109-127.
48. L. Šmejkal, J. Sinova, and T. Jungwirth, *Phys. Rev. X*, 2022, **12**, 040501.
49. C. Song, H. Bai, Z. Zhou, L. Han, H. Reichlova, J. Dil, J. Liu, X. Chen, and F. Pan, *Nat. Rev. Mater.*, 2025, **10**, 473-485.